CHEMISTRY
A EUROPEAN JOURNAL

DOI: 10.1002/chem.200500156

Mononuclear, Dinuclear, and Pentanuclear [{N,S(thiolate)}Iron(II)] Complexes: Nuclearity Control, Incorporation of Hydroxide Bridging Ligands, and Magnetic Behavior

Divya Krishnamurthy,[a] Amy N. Sarjeant,[a] David P. Goldberg,*[a] Andrea Caneschi,[b] Federico Totti,[b] Lev N. Zakharov,[c] and Arnold L. Rheingold[c]

Abstract: The mixed N_3S(thiolate) ligand 1-[bis{2-(pyridin-2-yl)ethyl}amino]-2-methylpropane-2-thiol (Py_2SH) was used in the synthesis of four iron(II) complexes: $[(Py_2S)FeCl]$ (**1**), $[(Py_2S)FeBr]$ (**2**), $[(Py_2S)_4Fe_5^{II}(\mu\text{-}OH)_2](BF_4)_4$ (**3**), and $[(Py_2S)_2Fe_2^{II}(\mu\text{-}OH)]BF_4$ (**4**). The X-ray structures of **1** and **2** revealed monomeric iron(II)–alkylthiolate complexes with distorted trigonal-bipyramidal geometries. The paramagnetic ^1H NMR spectra of **1** and **2** display resonances from $\delta = -25$ ppm to $+100$ ppm, consistent with a high-spin iron(II) ion ($S=2$). Spectral assignments were made on the basis of chemical shift information and T_1 measurements and show the monomeric structures are intact in solution. To provide entry into hydroxide-containing complexes, a novel synthetic method was developed involving strict aprotic conditions and limiting amounts of H_2O. Reaction of Py_2SH with NaH and $Fe(BF_4)_2{\cdot}6H_2O$ under aprotic conditions led to the isolation of the pentanuclear, μ-OH complex **3**, which has a novel dimer-of-dimers type structure connected by a central iron atom. Conductivity data on **3** show this structure is retained in CH_2Cl_2. Rational modification of the ligand-to-metal ratio allows control over the nuclearity of the product, yielding the dinuclear complex **4**. The X-ray structure of **4** reveals an unprecedented face-sharing, biooctahedral complex with an $[S_2O]$ bridging arrangement. The magnetic properties of **3** and **4** in the range 1.9–300 K were successfully modeled. Dinuclear **4** is antiferromagnetically coupled [$J = -18.8(2)$ cm^{-1}]. Pentanuclear **3** exhibits ferrimagnetic behavior, with a high-spin ground state of $S_T=6$, and was best modeled with three different exchange parameters [$J=-15.3(2)$, $J'=-24.7(3)$, and $J''=-5.36(7)$ cm^{-1}]. DFT calculations provided good support for the interpretation of the magnetic properties.

Keywords: cluster compounds · enzyme models · magnetic properties · S ligands · tripodal ligands

Introduction

In recent years there has been significant interest in the synthesis and study of transition-metal thiolate complexes. Zinc,[1–7] nickel,[8–12] and iron[13–20] thiolate complexes have been made as models for mononuclear and polynuclear metalloenzyme active sites with RS–M coordination. The alkylthiolate functionality is important because of its relevance to cysteinate ligation, but it is also quite challenging to control from a synthetic perspective. The challenges that arise include the avoidance of oxidative pathways that generate disulfide or sulfur-oxygenate species, as well as the control over the nuclearity of the final metal products. This latter issue originates from the propensity of alkylthiolate ligands to form indiscriminate bridges between metal ions.

Our research group has an ongoing effort in the synthesis and reactivity of alkylthiolate-containing metal complexes.

[a] D. Krishnamurthy, Dr. A. N. Sarjeant, Prof. D. P. Goldberg
Department of Chemistry, Johns Hopkins University
3400 N. Charles Street, Baltimore, MD 21218 (USA)
Fax: (+1) 410-516-8420
E-mail: dpg@jhu.edu

[b] Prof. A. Caneschi, Dr. F. Totti
Dipartimento di Chimica e UdR INSTM di Firenze
Polo Scientifico, Via della Lastruccia 3
50019 Sesto Fiorentino (Italy)

[c] Dr. L. N. Zakharov, Prof. A. L. Rheingold
Department of Chemistry and Biochemistry
University of California San Diego
9500 Gilman Drive, La Jolla, CA 92093 (USA)

Supporting information for this article is available on the WWW under http://www.chemeurj.org/ or from the author.

We are in part motivated by an interest in building models for metalloenzyme active sites, such as those found in the iron-containing enzymes peptide deformylase, superoxide reductase, and nitrile hydratase. Herein we describe the synthesis of four new alkylthiolate–iron(II) complexes with the tetradentate ligand 1-[bis{2-(pyridin-2-yl)ethyl}amino]-2-methylpropane-2-thiol (Py_2SH), which bears two pyridine donors, and one amine and one alkylthiolate donor. This ligand was previously synthesized for use in biomimetic copper chemistry.[21,22] Given the relatively easy synthesis of Py_2SH, we were surprised to find that only the copper chemistry of this ligand had been investigated. Thus we were motivated to develop its iron chemistry and determine its geometric and nuclearity preferences for the iron(II) ion.

Reaction of this ligand with iron(II) halides gives the monomeric high-spin Fe^{II} complexes $[(Py_2S)FeX]$ (X = Cl, Br). In the case of iron, mononuclear alkylthiolate complexes are even less common than for other metals.[14,16,20,23,24] These complexes exhibit five-coordinate structures in which the Py_2S^- ligand coordinates in a tetradentate fashion, although the amine donor forms an unusually weak interaction with the metal center. Paramagnetic NMR data are presented to characterize the solution-state structures of these complexes.

The synthesis of $(Py_2S)Fe^{II}$–hydroxide complexes was also targeted because of our interest in modeling the active site of peptide deformylase, which contains a coordinated OH^-/H_2O ligand at an RS–Fe^{II} center. Traditional syntheses of $(L)_nM/OH$ complexes involve self-assembly[25–28] or substitution[29,30] reactions with excess OH^-/H_2O in protic solvents. Here we describe a new strategy involving aprotic conditions (THF) and a nearly stoichiometric amount of water to give the hydroxide-containing complexes $[(Py_2S)_4Fe_5(\mu\text{-}OH)_2](BF_4)_4$ (**3**) and $[(Py_2S)_2Fe_2(\mu\text{-}OH)]BF_4$ (**4**). Both of these complexes display unprecedented structural motifs for iron(II). The latter is a dinuclear, face-sharing bioctahedral complex with an unusual set of single-atom bridging groups comprising two thiolate S atoms and one hydroxide oxygen atom. The former complex, which is synthesized under almost identical conditions to those used for **4**, exhibits a pentanuclear, dimer-of-dimers type structure with a central iron(II) ion linking $Fe_2^{II}(\mu\text{-}OH)$ units. A surprisingly simple synthetic method was discovered that allows control over the formation of either the dimeric or pentameric species.

Given the high-spin nature of the iron(II) ions in **3** and **4**, their magnetic properties were worthy of investigation. Magnetic susceptibility studies have revealed antiferromagnetic coupling for the dimer **4**, and *ferrimagnetic* coupling for the pentamer **3**. Density functional calculations are also presented in support of the Heisenberg spin Hamiltonian model for complex **3** to rationalize the ferrimagnetic $S_T = 6$ ground state.

Results and Discussion

The synthesis of Py_2SH followed the method reported by Ohta and co-workers.[21] The commercially available starting material 2-vinylpyridine was converted to bis(2-pyridylethylamine) by treatment with NH_4Cl,[31] which was then reacted with neat 1,1-dimethylthiirane at 70 °C to afford the ligand Py_2SH. It was noticed during the purification of bis(2-pyridylethylamine) that a large amount of primary amine, 2-pyridylethylamine, had also formed in the NH_4Cl reaction. To improve the overall yield of Py_2SH, the 2-pyridylethylamine was recycled and treated with 2-vinylpyridine under acidic conditions to give an additional amount of bis(2-pyridylethylamine).[32]

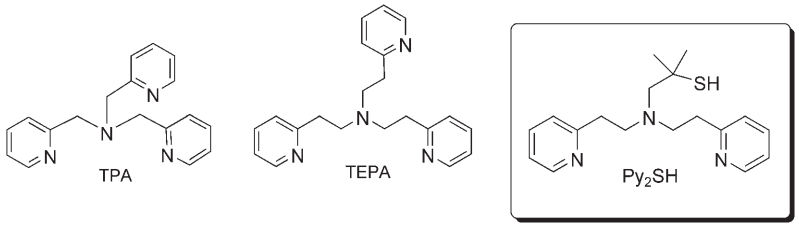

Synthesis of $[(Py_2S)FeCl]$ (1) and $[(Py_2S)FeBr]$ (2): Complexes **1** and **2** were synthesized by generation in situ of the deprotonated thiolate ligand, Py_2S^- with NaOH, followed by reaction with the appropriate ferrous halide starting material (Scheme 1). Complex formation was accompanied

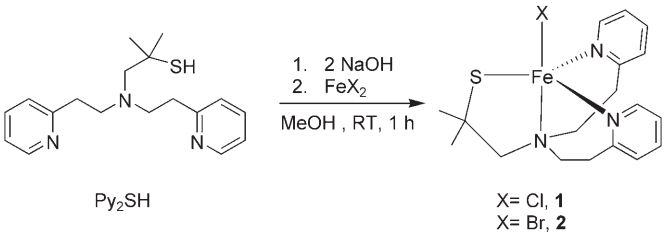

Scheme 1.

with the appearance of a bright yellow color. Vapor diffusion of diethyl ether into the filtered reaction mixtures yielded crystals of **1** and **2** suitable for X-ray diffraction. Strict anaerobic conditions must be maintained at all times for these complexes both in solution and in the solid state to prevent oxidation.

X-ray structures of 1 and 2: The molecular structures of $[(Py_2S)FeCl]$ (**1**) and $[(Py_2S)FeBr]$ (**2**) are shown in Figure 1 and Figure 2, respectively. Selected bond lengths and angles are given in Table 1. The structures of **1** and **2** show that Py_2S^- is capable of giving discrete, monomeric RS–Fe^{II} complexes, with the ligand coordinated in the expected tetradentate fashion. Both complexes exhibit distorted trigonal-bipyramidal geometries. The Fe^{II}–X (X = Br, Cl) and Fe–N_{py}

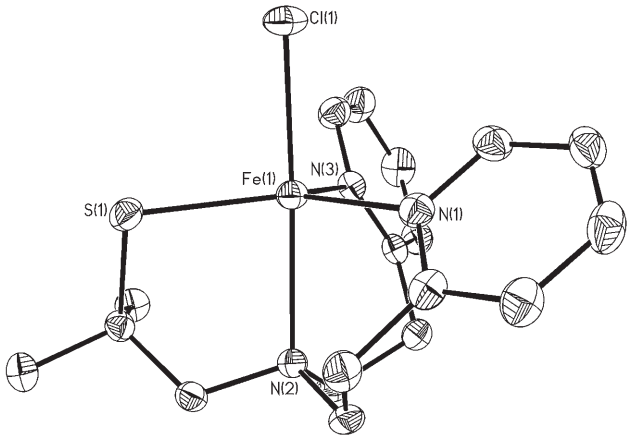

Figure 1. ORTEP diagram of [(Py_2S)FeCl] showing the 50% probability thermal ellipsoids. Hydrogen atoms have been omitted for clarity.

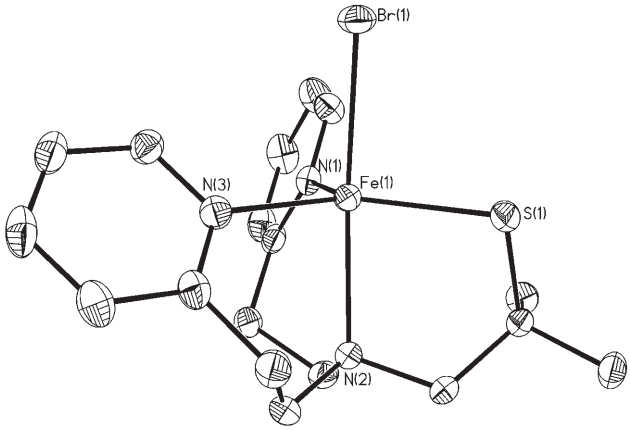

Figure 2. ORTEP diagram of [(Py_2S)FeBr] showing the 50% probability thermal ellipsoids. Hydrogen atoms have been omitted for clarity.

Table 1. Selected bond lengths [Å] and angles [°] for **1** and **2**.

Complex	**1** (X = Cl)	**2** (X = Br)
Fe–N(1)	2.1479(14)	2.1639(17)
Fe–N(2)	2.3875(13)	2.3521(16)
Fe–N(3)	2.1720(14)	2.1420(17)
Fe–S(1)	2.3274(5)	2.3212(5)
Fe–X(1)	2.4299(5)	2.6166(3)
N(3)-Fe-N(1)	105.36(5)	104.59(6)
N(3)-Fe-S(1)	133.35(4)	133.86(5)
N(1)-Fe-S(1)	120.20(4)	121.03(5)
N(3)-Fe-N(2)	89.29(5)	88.74(6)
N(1)-Fe-N(2)	87.47(5)	90.06(6)
N(3)-Fe-X(1)	96.67(4)	90.22(5)
N(1)-Fe-X(1)	90.59(4)	97.98(4)
S(1)-Fe-X(1)	93.458(17)	90.019(15)
N(2)-Fe-X(1)	174.03(4)	171.90(4)

bond lengths are in the normal range for high-spin iron(II) complexes,[33] with the average Fe^{II}–N_{py} distance of 2.160 Å for **1** and 2.152 Å for **2**. There are only a few examples of monomeric RS–Fe^{II} complexes for comparison. The Fe^{II}–SR distances for **1** and **2** are close to the Fe–SAr distance of 2.345(1) Å for [(TPA)Fe^{II}(SC_6H_2-2,4,6-Me_3)](ClO_4),[34] an iron(II) thiolate complex of the ligand TPA, and somewhat shorter than the salen complex (Et_4N)[Fe(5-NO_2salen)(S-*p*-tol)][35] with Fe^{II}–SAr = 2.386(2) Å. However, the series of recently syntheszied complexes [$L^8py_2Fe^{II}$(SR)]$^+$ (R = aryl, alkyl) exhibit Fe–SR bond lengths significantly shorter (ranging from 2.259(2)–2.323(3) Å) than in **1** and **2**, with the short end occupied by the *alkyl*thiolate (R = cyclohexyl) complex.[16]

The tertiary amine to iron(II) distances of 2.3875(13) Å and 2.3521(16) Å in **1** and **2**, respectively, are unusually long and deserve some comment. These distances are significantly longer than corresponding distances in the six-coordinate, high-spin (TPA)–Fe^{II} complexes [(TPA)Fe(BF)(MeOH)]ClO_4,[36] [(TPA)Fe(CH_3OH)$_2$](BPh_4)$_2$,[37] [(TPA)Fe(O_3SCF_3)$_2$],[37] and [(TPA)Fe(Cl)$_2$],[33] which exhibit Fe^{II}–N_{amine} distances of 2.175(6)–2.220(7) Å. A more analogous comparison to **1** and **2** would come from a series of five-coordinate TPA–iron(II) complexes, however there is only one example of a five-coordinate iron(II) species in which TPA binds in the typical tripodal mode, [(TPA)Fe(SC_6H_2-2,4,6-Me_3)]ClO_4,[34] and this complex has a normal Fe^{II}–N_{amine} bond length of 2.250(3) Å. The unusual eight-coordinate complex [(TPA)$_2$Fe](BPh_4)$_2$ is the only TPA complex to exhibit an Fe–N_{amine} distance (2.389(3) Å) as long as that of **1**,[37] but this elongated distance can be attributed to the crowded nature of the high-coordinate center.

Perhaps an even better comparison than TPA–Fe^{II} complexes for **1** and **2** are complexes of the ethylene-spaced TEPA (TEPA = tris(2-(2-pyridyl)ethyl)amine), but to our knowledge there are no examples of structurally characterized TEPA–Fe complexes. Out of the eight examples of transition metal–TEPA complexes in the Cambridge Structural Database,[38] none of them exhibit an unusually long M–N_{amine} bond.[39] Thus the cause of the significantly weakened N_{amine}–Fe^{II} interaction in **1** and **2** has not been conclusively determined. It is possible that the strong donating ability of RS^- combined with the presence of another negatively charged ligand (Cl^- or Br^-) reduces the positive charge on the iron center and thereby weakens the N_{amine} interaction, while the bonding between the py groups and Fe^{II} remains normal because of the π-acceptor ability of pyridine.

The angular parameters given in Table 1 show that both **1** and **2** are best described as distorted trigonal bipyramidal, in which the N_{amine} and halide ligands lie on the axial positions (N_{amine}-Fe-X: 174.03(4)° (**1**); 171.88(4)° (**2**)) and the two py and thiolate donors form the equatorial plane. Although the long Fe^{II}–N_{amine} distance in **1** and **2** suggests a weakened bonding interaction, the angles around the iron center clearly rule out a four-coordinate geometry. Angular data for five-coordinate complexes can be analyzed by calculation of a τ index,[40] with the limiting values of τ being 0.0 for square-pyramidal and 1.0 for trigonal-bipyramidal geometry. The τ indices for **1** and **2** are 0.68 and 0.63, respectively, showing that both compounds are closer to trigonal-bipyramidal than square-pyramidal.

^{1}H NMR spectroscopy: The ^{1}H NMR spectra for **1** and **2** are shown in Figure 3 and the data are summarized in Table 2. Both complexes exhibit paramagnetically shifted peaks between 100 to −25 ppm, which are typical for high-spin

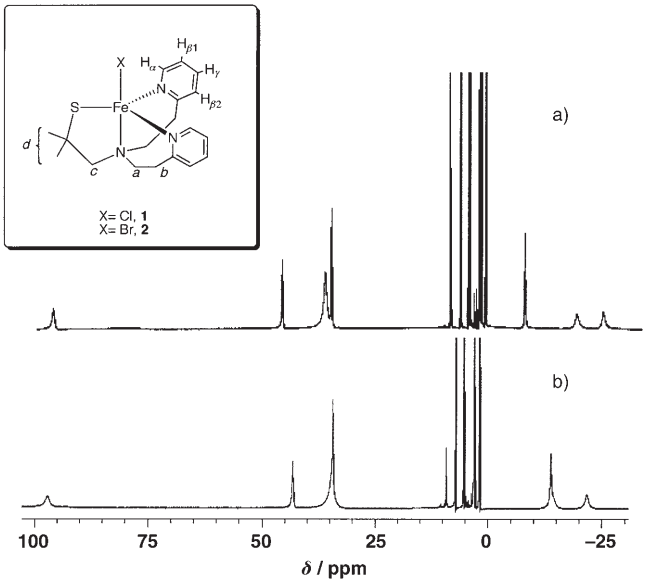

Figure 3. ^{1}H NMR spectra of a) **1** and b) **2** in CD_2Cl_2 at 25.0 °C. The peaks in the diamagnetic region (δ = 0–10 ppm) are due to trace solvent and trace amounts of free ligand.

Table 2. ^{1}H NMR chemical shifts and T_1 values for **1** and **2** in CD_2Cl_2 at 25 °C.

	1		**2**	
Proton	δ [ppm]	T_1 [ms]	δ [ppm]	T_1 [ms]
α	+90.9	1.8	+95.3	1.7
β_1,β_2	+42.9, +33.9	13.4, 25.0	+41.5, +32.5	14.8, 10.1[a]
γ	−8.2	39.2	−15.6	17.7[a]
a,*c*	+32.5	3.7	+32.5	10.1[a]
b	not assigned	–	not assigned	–
d	−19.0, −24.5	0.92, 1.87	−15.6, −23	17.7,[a] 0.98

[a] An "average" T_1 value for overlapping peaks (see text for discussion).

iron(II) complexes. Peak assignments have been made based on chemical shifts, T_1 measurements, and comparison with the literature. The spectra shown in Figure 3 are highly reproducible from batch to batch of **1** and **2**, and provide a good fingerprint for these complexes in solution. The farthest downfield shifted peaks at δ = 90.9 and 95.3 ppm for **1** and **2** are assigned to the α-protons, and have the shortest T_1 values among the pyridine protons, as expected based on proximity to the paramagnetic center. The peaks at δ = 42.9 and 41.5 ppm for **1** and **2**, respectively, are assigned to one of the H-β_1,β_2 protons. The other set of H-β_1,β_2 protons for **1** are assigned to the peak at δ = 33.9 ppm. Both H-β_1,β_2 protons in **1** exhibit T_1 values of similar magnitude (δ = 13.4 and 25.0 ms). In the case of the bromide complex, the other set of the H-β_1,β_2 protons is assigned to the relatively broad resonance at δ = 32.5 ppm, which overlaps with the methylene signals from H-*a* and H-*c*. In contrast, the H-*a*,*c* protons in **1** appear at 32.5 ppm as a separate peak. An assignable peak for the remaining methylene protons, H-*b*, was not found for either **1** or **2**. The γ protons in both **1** and **2** are shifted significantly upfield, appearing at δ = −8.2 and −15.6 ppm, respectively. They also have the longest T_1 values, consistent with literature values for H-γ, although the T_1 measurement for H-γ in **2** is an approximation because this peak lies on top of one of the *gem*-dimethyl peaks, H-*d* (the upfield shoulder at δ = −16 ppm). Distinct T_1 values for H-γ and H-*d* in **2** could not be obtained by the inversion-recovery method because of the overlap of these resonances, but the measured T_1 (17.7 ms) at δ = −15.6 ppm is close to an average of the T_1's for the analogous H-γ (39.2 ms) and H-*d* (0.92 ms) peaks for **1**. The remaining upfield-shifted peaks for **1** and **2** are assigned to the *gem*-dimethyl protons. For **1**, the *gem*-dimethyl groups appear at δ = −19.0 and −24.5 ppm. For **2**, one of the *gem*-dimethyl groups gives rise to the shoulder at δ = −16 ppm as mentioned above, while the other *gem*-dimethyl peak is a distinct, broad peak at δ = −23.0 ppm.

In solution, **1** and **2** may be expected to contain a mirror plane containing the Fe–S vector and bisecting the N_{py}-Fe-N_{py} angle, and the single set of pyridine resonances (H-α, H-β_1,β_2, H-γ) is consistent with this symmetry. However, the inequivalence of the *gem*-dimethyl groups suggests that this symmetry is broken by the -$CH_2C(CH_3)_2S^-$ arm. In the solid state (Figures 1 and 2), the *gem*-dimethyl groups are clearly inequivalent due to the conformation of the thiolate arm, and thus there may be conformational restriction of the -$CH_2C(CH_3)_2S^-$ group in solution, causing the separate peaks for H-*d* in the NMR spectra.[41]

The NMR assignments are based partly on comparison with the literature values for five-coordinate[33,34] and six-coordinate[33,36] monomeric TPA- and substituted TPA–Fe^{II} complexes. All of these complexes exhibit pyridine chemical shifts and $1/T_1$ values in the order H-α > H-β_1,β_2 > H-γ, and the assignments for **1** and **2** were based on this precedent. The chemical shifts for H-α in TPA–Fe^{II} species typically fall between δ = +110 to +140 ppm, with the upfield end of this range made up by the five-coordinate [(TPA)Fe(SAr)]$^+$ complexes reported by Zang and Que.[34] The relatively upfield-shifted H-α peaks for five-coordinate **1** and **2** match the trend for these species. The H-β_1,β_2 chemical shifts and T_1 values for **1** and **2** also fall in the same range as H-β_1,β_2 for other TPA–Fe^{II} species, which are found between δ = 23–65 ppm and exhibit T_1's of several milliseconds. The peak for H-γ in **1** and **2** appears farther upfield than in most TPA complexes, with the exception being the [(TPA)Fe(SAr)]$^+$ complexes (Hγ ~ −10 ppm), which are also the closest structural analogues to **1** and **2**. There is no direct precedent to compare the signals for the *gem*-dimethyl protons (H-*d*). The significant upfield shift of the H-*d* resonances may be explained by a spin delocalization mechanism, as opposed to a Fermi contact shift mechanism.[42]

Incorporation of OH^-: synthesis of $[(Py_2S)_4Fe^{II}_5(\mu\text{-}OH)_2](BF_4)_4$ (3): Complex **3** was synthesized by the deprotonation

of Py_2SH in dry, freshly distilled THF with sodium hydride, followed by reaction with a stoichiometric amount of $Fe(BF_4)_2{\cdot}6H_2O$ under inert atmosphere (Scheme 2). Recrystallization from CH_2Cl_2/pentane gave X-ray quality crystals, and a determination of the X-ray structure of **3** revealed a pentanuclear complex with two dimeric, $(Py_2S)_2Fe_2(\mu\text{-}OH)$ units organized around a central $Fe^{II}(\mu\text{-}SR)_4$ core (vide infra).

Typical methods of synthesizing $(L)_nM{-}OH$ species include substitution reactions, such as that between $[HB(pz^{tBu,Me})_3ZnI]$ and OH^- to give $[HB(pz^{tBu,Me})_3ZnOH]$,[28] and self-assembly reactions[25–27,43,44] in protic (e.g. MeOH) solvent. All of these strategies failed for the Py_2S^- system. For example, reaction of Py_2SH with $Fe(ClO_4)_2$ or $Fe(BF_4)_2$ in the presence of NaOH, KOH or Me_4NOH in MeOH did not lead to any tractable products. Attempts also were made to substitute the halide ligand of **1** and **2** with OH^-, but the only product was a dark green precipitate which was insoluble in most common organic solvents (e.g. CH_3CN, CH_2Cl_2 and MeOH) and could not be characterized further. These failures prompted us to attempt conditions in which the amount of H_2O/OH^- could be better controlled. Aprotic conditions (THF) combined with a limiting amount of H_2O from the $Fe(BF_4)_2{\cdot}6H_2O$ starting material led to the successful synthesis of the hydroxide species **3**, and the OH^- ligand in **3** occupies the open site of the $(Py_2S)Fe^{II}$ unit, as designed. These results suggest that the use of aprotic solvent combined with nearly stoichiometric amounts of H_2O can be a good approach for the preparation of other $(L)_nM^{II}{-}OH$ compounds.

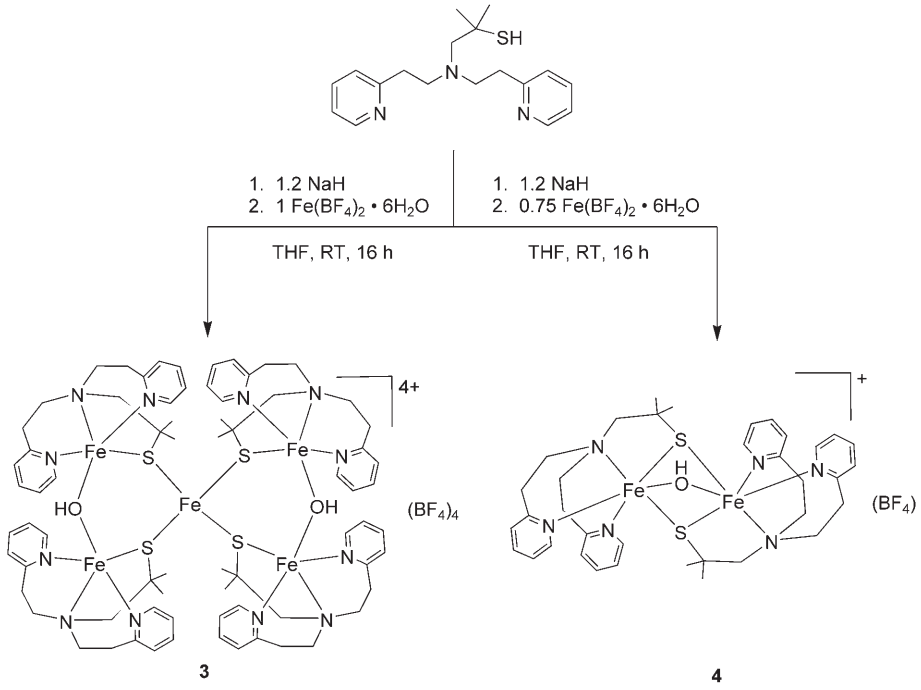

Scheme 2.

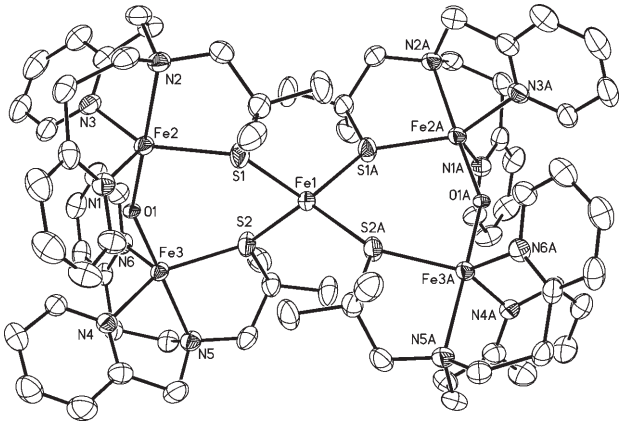

Figure 4. ORTEP diagram of the cation of $[(Py_2S)_4Fe_5(\mu\text{-}OH)_2](BF_4)_4$ (**3**) showing the 30% probability thermal ellipsoids. Hydrogen atoms and solvent molecules have been omitted for clarity.

Molecular structure of $[(Py_2S)_4Fe_5(OH)_2](BF_4)_4$ (3): The molecular structure of the cation in **3** is shown in Figure 4, and selected bond lengths and angles are given in Table 3. This molecule can be viewed as two $Fe^{II}{-}(\mu\text{-}OH){-}Fe^{II}$ complexes joined together by a central iron(II) ion (Fe1). The Fe1 ion is located on a crystallographically imposed twofold axis, and thus there is only one unique dimeric $Fe^{II}_2(\mu\text{-}OH)$ unit. Each iron center in the dimeric unit is five-coordinate and bridged by a single hydroxide ligand. The bridging atom is assigned to a hydroxide group based on $Fe^{II}{-}O$ bond lengths, charge balance considerations, and magnetic susceptibility data (vide infra). The chelating thiolate arms form four bridges to the central iron(II) ion, resulting in a distorted tetrahedral $Fe(SR)_4$ coordination sphere for Fe1. The hydroxide bridge is located *trans* to the tertiary amine group for both Py_2S^- ligands, and the N_{amine}-Fe-OH vector makes up the axial direction of a distorted trigonal-bipyramidal geometry for both Fe2 and Fe3.

The average $Fe{-}N_{pyridine}$ bond length of 2.11 Å in **3** is shorter than the $Fe{-}N_{pyridine}$ distances of the five-coordinate complexes **1** and **2**. Similarly, $d(Fe{-}N_{amine})_{av} = 2.29(1)$ Å in **3** is significantly smaller than the corresponding distance in **1** or **2**. Thus the unusually weak interaction between the N_{amine} and Fe^{II} seen in **1** and **2** is not observed in **3**. The RS^- and OH^- ligands in **3** both share their negative charge with two iron(II) ions, whereas in **1** and **2** the thiolate and X^- (X = Cl, Br) donors provide a full negative charge to a single iron(II) center, and therefore the resultant higher positive charge on

Table 3. Selected bond lengths [Å] and angles [°] for $3\cdot 2CH_2Cl_2\cdot C_5H_{12}$.

Fe1–S1	2.3134(11)	O1-Fe2-N1	92.21(10)
Fe1–S2	2.3182(10)	O1-Fe2-N3	86.48(10)
Fe2–O1	2.0140(18)	N1-Fe2-N3	114.10(12)
Fe2–N1	2.091(3)	N3-Fe2-N2	89.89(11)
Fe2–N2	2.296(3)	O1-Fe2-N2	175.27(10)
Fe2–N3	2.118(3)	N1-Fe2-N2	92.04(12)
Fe2–S1	2.3220(11)	O1-Fe2-S1	97.71(6)
Fe3–O1	2.0211(18)	N1-Fe2-S1	108.48(9)
Fe3–N4	2.126(3)	N3-Fe2-S1	137.02(10)
Fe3–N5	2.295(3)	N2-Fe2-S1	82.90(8)
Fe3–N6	2.106(3)	O1-Fe3-N6	92.30(10)
Fe3–S2	2.3375(11)	O1-Fe3-N4	86.75(10)
Fe2–Fe3	3.905	O1-Fe3-N5	174.86(10)
S1-Fe1-S1	116.79(7)	N6-Fe3-N4	110.43(12)
S1-Fe1-S2	116.13(4)	N6-Fe3-N5	92.51(11)
S1-Fe1-S2	94.18(3)	N4-Fe3-N5	89.87(12)
S2-Fe1-S2	121.36(6)	O1-Fe3-S2	96.20(6)
O1-Fe2-N1	92.21(10)	N6-Fe3-S2	109.24(9)
O1-Fe2-N3	86.48(10)	N4-Fe3-S2	140.06(9)
S1-Fe1-S1	116.79(7)	N5-Fe3-S2	83.92(8)
S1-Fe1-S2	116.13(4)	Fe2-O1-Fe3	150.8(1)
S1-Fe1-S2	94.18(3)	Fe1-S1-Fe2	137.74(5)
S2-Fe1-S2	121.36(6)	Fe1-S2-Fe3	135.39(5)

Fe2 and Fe3 in **3** may be the cause of the shorter N–Fe bond lengths. The same shortening is not observed in the Fe–SR distances for **3**, falling between 2.3134(11)–2.3375(11) Å, but the bridging mode of the thiolate donors is expected to lengthen the Fe–SR distances.

The Fe^{II}–(μ-OH) bonds in **3** are on the short end of Fe^{II}–(μ-OH) distances found in the literature, although these values are mainly for six-coordinate Fe^{II} complexes.[45,46] To our knowledge, there are only two complexes with five-coordinate iron(II) ions bridged by a hydroxide ligand: $[Fe^{II}(HB(3,5\text{-}i Pr_2pz)_3)]_2(OH)_2$, a bis(μ-hydroxo) complex, and $[Fe^{II}(HB(3,5\text{-}i Pr_2pz)_3)]_2(OH)(OBz)$, a μ-hydroxo, μ-carboxylato complex.[30] These complexes have Fe–(μ-OH) distances of 1.964–2.04 Å, and complex **3** fits well within this range. In contrast, the Fe–Fe distance of 3.905 Å in **3** is much longer than that in either $[Fe^{II}(HB(3,5\text{-}i Pr_2pz)_3)]_2(OH)_2$ (Fe–Fe 3.179(5) Å) or $[Fe^{II}(HB(3,5\text{-}i Pr_2pz)_3)]_2(OH)(OBz)$ (Fe–Fe 3.681(3) Å), and can be correlated with the obtuse Fe-OH-Fe angle 150.8(1)°. Such a wide angle is found in (porphyrinoid)M-(μ-OH)-M(porphyrinoid) structures,[47,48] which have only one bridging ligand connecting the metal centers, as opposed to **3**, which has the S1-Fe1-S2 unit as a second bridge between Fe2 and Fe3. The long Fe–S distances likely allows for the unusually obtuse Fe2-(μ-OH)-Fe3 angle. The related $[Fe^{II}(HB(3,5\text{-}i Pr_2pz)_3)]_2(OH)(OBz)$ has a tighter, more rigid second bridge in the form of OBz, and consequently has a smaller Fe^{II}-(μ-OH)-Fe^{II} angle of 137.0(3)°, in agreement with the μ-hydroxo, μ-carboxylato motif.[49,50]

The angles around Fe2 and Fe3 reveal distorted trigonal-bipyramidal geometries for both metal ions. The angle between the N_{amine} donor and the hydroxide bridge for each iron is 175.27° and 174.86°, consistent with the axial direction of a trigonal bipyramid. However, significant deviations from 120° occurs in the equatorial plane formed by the two pyridine and thiolate donors on each iron, and these deviations are reflected in the τ values, which are 0.63 for Fe2 and 0.58 for Fe3. Considerable distortion from tetrahedral geometry is also observed for Fe1, with angles ranging from 121.36(6)° to 94.18(3)°.

Solution-state structure of $[(Py_2S)_4Fe_5(OH)_2](BF_4)_4$ (3): *Conductivity*: The X-ray structure of **3** shows a $[(Py_2S)_4Fe_5(\mu\text{-}OH)_2]^{4+}$ ion with four BF_4^- counterions, and therefore it should behave as a 1:4 electrolyte in solution if the solid-state structure remains intact. Electrical conductivity measurements of **3** were carried out in CH_2Cl_2 to characterize the nature of the complex in solution.[51–53] Conductivity measurements are often done in more polar solvents such as H_2O, CH_3CN and CH_3OH, especially with 1:4 electrolytes,[54,55] but these solvents were not used because they could potentially coordinate to the iron(II) ions in **3** and disrupt the structure of the Fe_5 cluster. Since **3** was crystallized from CH_2Cl_2, it was the solvent of choice for conductivity measurements. Figure S1 in the Supporting Information shows the Onsager plots of compound **3**, and of the reference compound $[nBu_4N]PF_6$, which was used as a standard 1:1 electrolyte. The slope for **3** (slope = 2913) is close to four times that of the reference, $[nBu_4N]PF_6$ (slope = 627), suggesting that **3** behaves as a 1:4 electrolyte in CH_2Cl_2, and that the $[(Py_2S)_4Fe_5(\mu\text{-}OH)_2]^{4+}$ unit remains intact in solution. These results are also consistent with the ^1H NMR spectrum for **3** (see Experimental Section), which shows a complex pattern of paramagnetically shifted resonances, quite distinct from the relatively symmetric NMR spectra for **1** and **2**.

Control of nuclearity: **Synthesis of $[(Py_2S)_2Fe_2^{II}(\mu\text{-}OH)](BF_4)$ (4)**: Inspection of the structure of the pentanuclear complex **3** suggested that removal of the central Fe^{II} ion should lead to the isolation of the dinuclear $(Py_2S)_2Fe_2^{II}(\mu\text{-}OH)$ unit. Given that the overall metal/ligand ratio in **3** is 5:4, we speculated that limiting the Fe^{II} to substoichiometric quantities might lead to the synthesis of the dinuclear $[(Py_2S)_2Fe_2^{II}(\mu\text{-}OH)]$ complex. When the reaction was run with a $Py_2SH/NaH/Fe(BF_4)_2\cdot 6H_2O$ ratio of 1/1/0.75 in THF, a yellow precipitate formed immediately as in the case of **3**. However, vapor diffusion of pentane into a solution of the crude material in CH_2Cl_2 led to the crystallization of a different product. Analysis of this compound by X-ray diffraction revealed complex **4**, which has the intended hydroxide-bridged, dinuclear structure, although the thiolate ligands that previously were bound to the central Fe^{II} ion in **3** are now bridged to the opposite iron(II) ion in the dimer (Scheme 2). Crystals of **3** and **4** are easily distinguishable by eye due to differences in their morphology (needles versus blocks).

Molecular structure of $[(Py_2S)_2Fe_2(\mu\text{-}OH)](BF_4)$ (4): An ORTEP diagram of the dinuclear complex **4** is shown in Figure 5, and selected bond lengths and angles are given in Table 4. The structure is best described as a face-sharing bio-

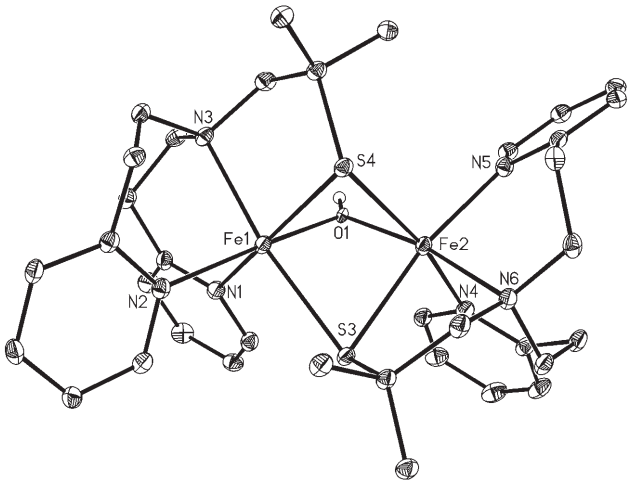

Figure 5. ORTEP diagram of the cation of $[(Py_2S)_2Fe_2(\mu\text{-}OH)](BF_4)$ (**4**) showing the 30% probability thermal ellipsoids. Hydrogen atoms and solvent molecules have been omitted for clarity.

Table 4. Selected bond lengths [Å] and angles [°] for **4**.

Fe1–O1	2.1613(16)	O1-Fe1-S3	83.84(5)
Fe1–S3	2.5074(9)	N1-Fe1-S4	161.73(6)
Fe2–O1	1.9842(16)	N2-Fe1-S3	97.38(6)
Fe1–N1	2.290(2)	N3-Fe1-S3	171.78(6)
Fe1–N2	2.188(2)	N1-Fe1-S3	92.81(6)
Fe1–N3	2.256(2)	S4-Fe1-S3	90.48(3)
Fe1–S4	2.4406(9)	O1-Fe2-N5	101.72(8)
Fe2–S4	2.6708(9)	O1-Fe2-N6	168.73 (7)
Fe2–N4	2.256(2)	N6-Fe2-N5	89.33 (8)
Fe2–N5	2.155(2)	N4-Fe2-N5	86.89(8)
Fe2–N6	2.249(2)	O1-Fe2-N4	90.54 (8)
Fe2–S3	2.5078(8)	N6-Fe2-N4	92.34 (8)
Fe1–Fe2	2.9288	O1-Fe2-S3	87.52 (5)
Fe2-O1-Fe1	89.80(6)	N5-Fe2-S3	169.68 (6)
O1-Fe1-N2	166.53(7)	N6-Fe2-S3	81.66(6)
O1-Fe1-N3	90.82(7)	N4-Fe2-S3	88.46(6)
N2-Fe1-N3	89.26(8)	O1-Fe2-S4	81.15(5)
O1-Fe1-N1	78.97(7)	N5-Fe2-S4	100.43(7)
N2-Fe1-N1	87.58(8)	N6-Fe2-S4	94.74(6)
N1-Fe1-N3	92.29(8)	N4-Fe2-S4	169.86(6)
O1-Fe1-S4	83.54(5)	S4-Fe2-S3	85.39(3)
N2-Fe1-S4	109.829(6)	Fe1-S3-Fe2	71.46(2)
N3-Fe1-S4	82.69(6)	Fe1-S4-Fe2	69.65(2)

octahedral complex, in which the two iron centers are joined by two bridging thiolate groups and one bridging hydroxide ligand. Face-sharing biooctahedral complexes of the type $L_3M(\mu\text{-}X)_3ML_3$ form a large and well-studied group of molecules.[56–58] However, to our knowledge there are no examples of complexes in which two iron atoms share one O and two S bridging atoms. The $Fe_2(RS)_2(O)$ core also reveals a striking asymmetry in the Fe^{II}–OH bond lengths. The Fe1–OH distance is 2.161(2) Å, and is one of the longest Fe^{II}–OH bonds reported, while the Fe2–OH distance of 1.984(2) Å is one of the shortest.[45] The long Fe^{II}–OH bond in **4** is *trans* to the short pyridine bond Fe1–N2 (2.188(2) Å), and the short Fe^{II}–OH interaction is *trans* to the longer tertiary amine bond Fe2–N6 (2.249(2) Å). Thus the asymmetry in the Fe^{II}–(μ-OH)-Fe^{II} unit may be a consequence of *trans* effects. All but one of the Fe-S distances are in the range 2.44–2.51 Å and are similar to other bridging thiolate distances in related $Fe^{II}_2(\mu\text{-}SR)_2$ complexes.[59] The Fe2–S4 distance is significantly longer at 2.67(1) Å, and although the reason for this long distance is not clear, it may be a consequence of steric strain.

An Fe–Fe distance of 2.929(1) Å is observed for **4**, and is shorter than other high-spin Fe^{II}_2 face-sharing bioctahedra, such as $[(tacn)Fe^{II}(\mu\text{-}Cl)_3Fe^{II}(tacn)]^+$ (Fe–Fe 3.014(2) Å; tacn = 1,4,7-triazacyclononane) prepared by Wieghardt et al.[60] or $[(thf)Fe^{II}(\mu\text{-}Cl)_3Fe^{II}(thf)]^+$ (Fe–Fe 3.086(2) Å) prepared by Sobota et al.[61] However, it is significantly longer than in related metal–metal bonded species such as $Fe^{II}_2(S_2C_3H_6)(CNMe)_7]^+$ (Fe–Fe 2.634(2) Å).[62] The relatively long Fe–Fe distance, combined with the paramagnetic behavior of **2** (vide infra), clearly rules out the presence of a metal–metal bond in **4**.

It is tempting to suggest complex **4** is formed by the fusion of two distinct monomeric species based on the asymmetry observed in the X-ray structure. One species could be a terminal hydroxide complex containing Fe2, in which the OH ligand is coordinated *trans* to the tertiary amine as found for the other X^- ligands (X = Cl, Br, OH) in **1**–**3**, while the other species could be a solvento complex of Fe1 with THF coordinated in the same site. Upon bringing the two monomers together, the weakly bound THF on Fe1 is displaced by the thiolate donor S(2), and the terminal hydroxide ligand makes a weak bridging interaction with Fe1. The third bridge is formed between the remaining thiolate ligand S4 and Fe2.

The synthesis and structural characterization of **3** and **4** provides an example of how subtle changes in a reaction system can influence the nuclearity and arrangement of transition metal complexes. Synthetic control over nuclearity is usually difficult to achieve, yet it is important in order to build molecules of defined metal ion content, spatial arrangement, and physical properties. It is especially important for paramagnetic metal ions such as high-spin iron(II), because of their application in the field of molecular magnetism, for which the rational synthesis of polynuclear complexes with new topologies and interesting magnetic properties is a central theme.[63–65] The magnetic properties of both **3** and **4** are presented below.

Magnetic properties of $[(Py_2S)_2Fe_2(\mu\text{-}OH)]BF_4$ (4): The magnetic susceptibility data for **4** are presented in Figure 6 as a χT versus T plot. At room temperature, the product of χT is 5.85 emu K mol^{-1}, which is approaching the spin-only value for two independent high-spin Fe^{II} (d^6) $S = 2$ ions. As the temperature is decreased, there is a steady decrease in χT down to the final value of 0.043 emu K mol^{-1} at 1.9 K. This behavior is consistent with intramolecular antiferromagnetic coupling between the two high-spin Fe^{II} ions, resulting in a non-magnetic ground state.

The experimental data in Figure 6 was fit to the model shown in Equation (1), which was derived from the spin Hamiltonian for two interacting $S = 2$ ions ($H = -2JS_1S_2$).

$$\chi T = \left(\frac{Ng^2\beta^2}{3k}\right)\frac{2\exp\left(\frac{J}{kT}\right)+10\exp\left(\frac{3J}{kT}\right)+28\exp\left(\frac{6J}{kT}\right)+60\exp\left(\frac{10J}{kT}\right)}{1+3\exp\left(\frac{J}{kT}\right)+5\exp\left(\frac{3J}{kT}\right)+7\exp\left(\frac{6J}{kT}\right)+9\exp\left(\frac{10J}{kT}\right)} \quad (1)$$

All symbols have the usual meaning. A least-squares fit of the data in Figure 6 using Equation (1) gives $J=-18.8(2)\ cm^{-1}$, $g=2.187(5)$, and $R^2=0.99938$. As seen in Figure 6, the fit is quite good and it is not necessary to include a term accounting for paramagnetic impurities. Although there are few examples of high-spin iron(II) face-sharing, biooctahedral complexes, the magnetic properties of the complexes from Wieghardt et al. ($[(tacn)Fe^{II}(\mu\text{-}Cl)_3Fe^{II}(tacn)]^+$) and Sobota et al. ($[(thf)Fe^{II}(\mu\text{-}Cl)_3Fe^{II}(thf)]^+$) have been studied in detail.[60,61] The $[(thf)Fe^{II}(\mu\text{-}Cl)_3Fe^{II}(thf)]^+$ complex was found to be weakly antiferromagnetically coupled, with $J=-4.6\ cm^{-1}$. In contrast, the $[(tacn)Fe^{II}(\mu\text{-}Cl)_3Fe^{II}(tacn)]^+$ complex was determined to be weakly *ferromagnetically* coupled, with $J=+11.6\ cm^{-1}$. Ferromagnetic coupling is unusual in these types of dimers, and this molecule appears to be an anomaly in terms of its magnetic behavior. It should be noted that best fits for both of these complexes included contributions from zero field splitting ($1.0<|D|<5.5\ cm^{-1}$).[60] It was not necessary to include zero-field splitting (zfs) terms for **4** in order to obtain an excellent fit (Figure 6), and given the larger J value for **4** it seems reasonable to ignore the small zfs terms.

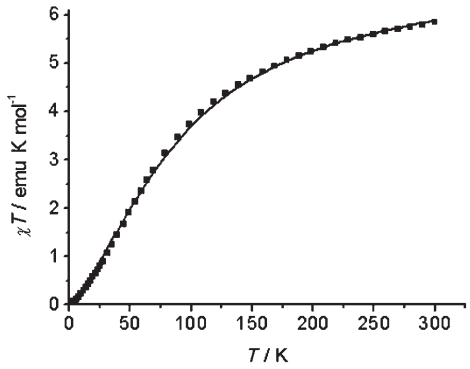

Figure 6. Plot of χT versus T for complex **4**. The solid line is the best fit obtained from the analytical expression described in the text.

The antiferromagnetic coupling in **4** is quite similar to that in the $Fe^{II}_2(\mu\text{-}SR)_2$ complex $[(L_c)_2Fe^{II}_2(NO_3)_2]$ (HL_c = 2-[[2-(2-pyridyl)ethyl]amino]ethanethiol)), which has $J=-20.04(4)\ cm^{-1}$, $g=2.137(2)$.[59] The only superexchange pathways for the latter complex come from the bridging alkylthiolate groups, and the similarity of the coupling in this complex and that found for **4** suggest that the alkylthiolate bridges in **4** provide the dominant exchange pathways, making the hydroxide bridge superfluous with regards to mediating the antiferromagnetic coupling. This analysis is reasonable in light of the fact that the Fe–(μ-SR) bonding in **4** should be more covalent than the Fe–(μ-OH) interactions. The antiferromagnetic coupling in the mixed-valent dimer $[(Fe_2(OH)_3(tmtacn)]^+$ (tmtacn = trimethyltriazacyclononane) is weaker than in the mixed-valent dimers of the type $[Fe_2S_2]^+$, and this phenomenon has been explained in part by the greater covalency of the S^{2-} bridges.[66]

Magnetic properties of $[(Py_2S)_4Fe_5(OH)_2](BF_4)_4$ (3): The magnetic susceptibility for **3** was recorded over a temperature range of 2–300 K. The temperature dependence of the χT product for complex **3** is shown in Figure 7. The high-temperature value of χT is below the value for five noninteracting iron(II) ions (15.0 emu K mol^{-1} for $g=2.00$), and a minimum in χT is seen near 250 K, which are indications of a ferrimagnetic species. A monotonic increase in χT is observed upon decreasing the temperature, leading to a maximum of 21.24 emu K mol^{-1} at 19 K, which is close to the value expected for a system with $S_T=6$ (22.5 emu K mol^{-1}). Below 19 K, χT rapidly decreases to 5.5 emu K mol^{-1} at 2 K. This decrease at low temperatures may be due to zero-field splitting contributions, intercluster magnetic interactions, or saturation effects. The gross behavior of the curve suggests an antiferromagnetic arrangement of iron(II) ions with a ferrimagnetic ground state of $S_T=6$.

To confirm this qualitative interpretation, a least-squares fit of the data in Figure 7 was carried out, providing values for the different exchange parameters. As a first approximation, the degeneracy and spin-orbit contributions arising from the ^5D ground state of a high-spin ferrous ion were neglected, and a single g value for all of the iron ions was employed. Taking into account the twofold symmetry of the cluster, three different exchange pathways can be individuated: two different pathways are mediated by a sulphur bridge (J and J') and one pathway is mediated by a hydroxo bridge (J''). The spin Hamiltonian shown in Equation (2) was used, with negative J indicating antiferromagnetism and positive J indicating ferromagnetism. Least-squares fits

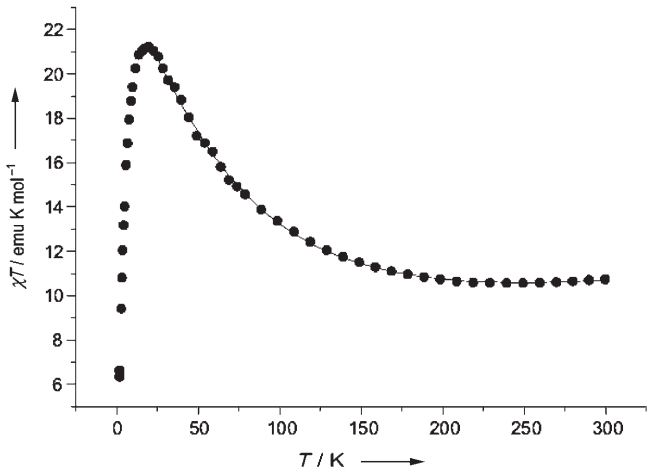

Figure 7. Plot of χT versus T for complex **3**. The solid line is the best fit obtained from a full-matrix diagonalization.

of the data were obtained by using a full-matrix diagonalization of the model given in Equation (2).[67]

$$H = -2J(S_1S_2 + S_1S_{2A}) - 2J'(S_1S_3 + S_1S_{3A}) - 2J''(S_2S_3 + S_{2A}S_{3A}) \quad (2)$$

Fits of the data in Figure 7 invariably gave negative J values for all three exchange interactions, indicating antiferromagnetic interactions between all of the iron(II) ions. Stronger antiferromagnetic exchange was found for the two sulfur-mediated pathways as compared to the hydroxo-bridged pathway. Different fits of the data between 19 K and 300 K of almost equivalent quality could be obtained by changing the starting values of the parameters, resulting in significantly different final J, J', J'' values. Nearly equivalent fits were found with different J/J' ratios, ranging from fit 1: $J/J' = 1$, $g = 2.10(2)$, $J = J' = -20(1)\ cm^{-1}$, $J'' = -6.7(3)\ cm^{-1}$ with $R = 2.05 \times 10^{-4}$, to fit 2: $J/J' = 1.6$, $g = 2.078(2)$, $J = -15.3(2)\ cm^{-1}$, $J' = -24.7(3)\ cm^{-1}$, $J'' = -5.36(7)\ cm^{-1}$ with $R = 1.77 \times 10^{-4}$ ($R = \Sigma\frac{(\chi_{obs} - \chi_{calcd})^2}{\chi_{obs}^2}$). For all initial J/J' ratios the value of J'' was consistently determined to be about $-6\ cm^{-1}$.

Thus this fitting procedure did not allow us to distinguish between a model in which the two sulfur bridges mediate nearly equivalent superexchange interactions versus a model in which they show quite different coupling efficiencies. The metrical parameters for each sulfur bridge show some small differences, with Fe1–S1 2.313(1), Fe1–S2 2.318(1), Fe2–S1 2.322(1), Fe3–S2 2.337(1), Fe1–Fe2 4.324, Fe1–Fe3 4.307 Å and Fe1-S1-Fe2 137.7 and Fe1-S2-Fe3 135.5°. These small differences allow for the possibility that these pathways could exhibit substantially different exchange coupling.

To gain further insight into this problem, quantum mechanical calculations were performed based on the density functional theory (DFT) in the B3LYP-broken symmetry[68,69] framework. A Gaussian type Ahlrichs TVZ basis set was used for the iron atom while Ahlrichs VDZ basis sets were used for the S, N, O, and H atoms. The NWChem 4.6 package[70,71] was used. The crystallographically imposed twofold symmetry of **3** allowed the simplified model shown in Figure 8 to be used for all of the calculations, in which symmetry-equivalent atoms were omitted. The *gem*-dimethyl groups of the two unique Py_2S^- ligands were also omitted in order to simplify the calculations. Hydrogen atoms were used in place of the two symmetry-related iron atoms to satisfy the sulfur valences. The following spin Hamiltonian was used [Eq. (3)]:

$$H = -2J(S_1S_2) - 2J'(S_1S_3) - J''(S_2S_3) \quad (3)$$

We computed three broken symmetry determinants[72] in addition to the high spin case (see Table 5) to obtain the three exchange parameters J, J', and J''. This calculation leads to a determinate system of three equations with three variables, and the solution of such a system gives the following values: $J = -15.4\ cm^{-1}$, $J' = -23.2\ cm^{-1}$, and $J'' = -22.3\ cm^{-1}$. All of the computed J values are antiferromagnetic, in agreement with the experimental findings. The calculated J and J' values are in good agreement with the values obtained from the experimental fit 2, which gave inequivalent exchange interactions for the two sulfur bridges. However, the calculated value of J'' is significantly larger than that found through fitting the experimental data. Despite this discrepancy, the computed J values suggest that the best fit of the experimental data includes inequivalent J and J' parameters.

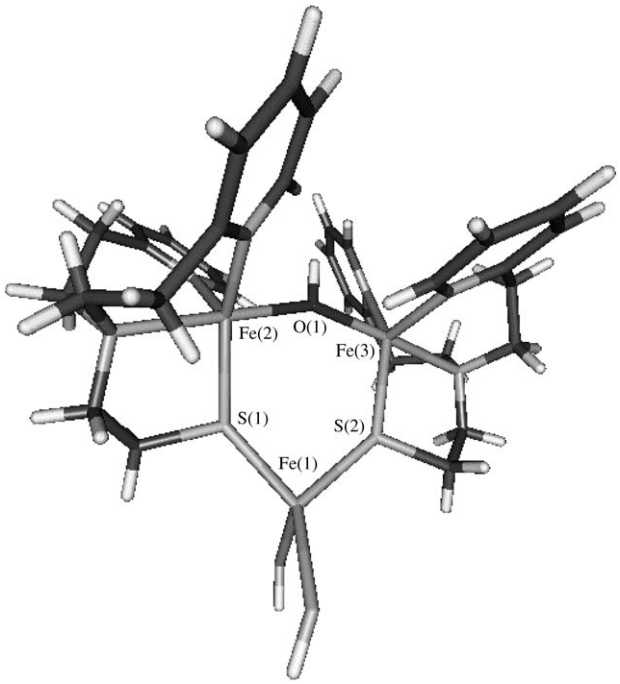

Figure 8. The model geometry of **3** used for density functional calculations.

Table 5. Determinants, SCF energies, and expectation values of $\langle \hat{S}^2 \rangle$, expected and computed (in parenthesis), for compound **3**. Only determinants with positive M_s were reported.

	State/M_s	$\langle \hat{S}^2 \rangle$	SCF energy [a.u.]
HS:	$\|222\rangle; M_s = 6$	40.00 (40.09)	−7030.093412
BS1:	$\|\bar{2}22\rangle; M_s = 2$	10.00 (10.06)	−7030.096229
BS2:	$\|22\bar{2}\rangle; M_s = 2$	10.00 (10.05)	−7030.096162
BS3:	$\|2\bar{2}2\rangle; M_s = 2$	10.00 (10.04)	−7030.096733

In light of the DFT results, a spin-Hamiltonian analysis of the magnetic structure was done using the set of parameters from fit 2. An $S_T = 6$, $|446>$ (where $|S_A S_{A'} S_T>$, with $S_A = S_2 + S_3$ and $S_{A'} = S_{2'} + S_{3'}$) was found to be the ground state. The first excited state is $28.6\ cm^{-1}$ above the ground state. The picture of the magnetic structure of **3** that emerges from these calculations is shown in Figure 9. The picture shows that Fe(2) and Fe(3) (and their symmetry related ions) are ferromagnetically polarized by the stronger J and J' exchange pathways, in spite of the presence of intrinsic antiferromagnetism in the magnetic exchange parameter J''.

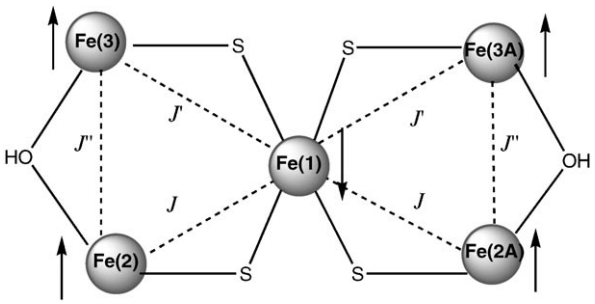

Figure 9. Spin topology for **3** derived from fitting the experimental data.

The $S_T=6$ ground state is clearly a result of competing exchange interactions.

To shed more light on the magnetic structure of complex **3**, we calculated the dependence of the spin frustration as a function of the exchange parameters. The eigenvalues for various ground states as a function of the ratio $\rho=((J + J')/2)/J''$, with J/J' fixed to the experimental value of 0.62 (see fit 2), are shown in Figure 10. At $\rho=3.7$, the competing exchange pathways result in a reversal of the intrinsic antiparallel character of J'' and give rise to a well-separated ground state ($S_T=6$) with parallel spin alignment of the outer iron ions, as shown in Figure 9. As ρ varies from the experimental ratio of 3.7 to 1, the system tends to have a more frustrated magnetic structure and an associated decrease of S_T values. On moving to ρ values of 2 to 1/3, quasi-degenerate ground states are found in which the uniform parallel alignment of the outer spins is no longer observed, indicating significant spin frustration. The $S_T=0$ state becomes the ground state for $\rho=2$. For $\rho=1$, as expected for three competing antiferromagnetic exchange pathways with similar magnitude,[73] $S_T=0$ is only 1.1 cm^{-1} above the $S_T=2$ ground state.

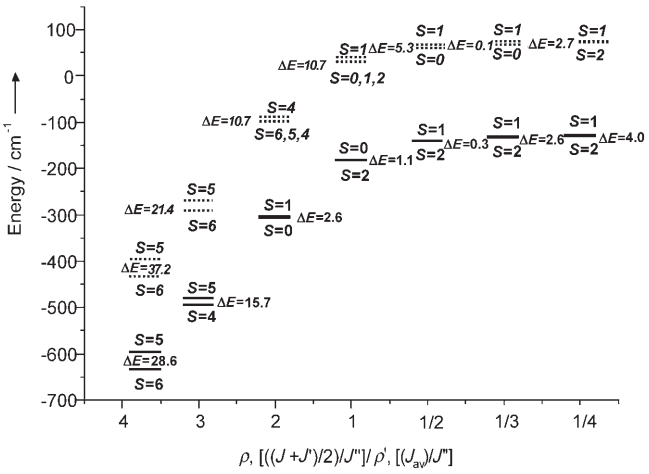

Figure 10. Plot of the variation of the energy of the ground state and the first excited state as a function of $[(J + J')/2]/J''$, with the J/J' ratio fixed at 0.62 (solid line). The variation of the energy is also reported for $\rho'=[(J_{av}')/2]/J''$, with $J_{av}=J + J'$ and ratio fixed at 1.0 (dotted line).

The variation of eigenvalues as a function of $\rho'=J_{av}/J''$ where $J_{av}=(J + J')/2$, with fixed $J/J'=1$, was also calculated (Figure 10) to check how much the discrepancy between J and J' influences the magnetic structure. In this case, a high spin ground state ($S_T=6$) is retained from $\rho'=4$ down to $\rho'=2$. Accidentally degenerate situations are observed for $\rho'<3$; the system, therefore, can be described in this case as experiencing a truly "spin-frustrated" situation in which the competing exchange interactions lead to a degenerate ground state.[74] For $\rho'=2$, an accidentally degenerate ground state is predicted where different spin states with $S_T=4$, 5, 6 have the same energies. For $\rho'=1$, all of the magnetic interactions have the same magnitude, and again an accidentally degenerate ground state is calculated, this time with spin states $S_T=0$, 1, 2. Only for $\rho'=1/4$ is a relatively separated ground state ($S_T=2$) predicted.

From the previous analyses we can conclude that for most combinations of J, J', and J'', J and J' must be much higher than J'' to have a ground state with $S_T=6$. However, for the case in which $J=J'$, an isolated $S_T=6$ ground state can be obtained with a smaller ratio ($\rho' < \rho$). The experimental and theoretical results for complex **3** provide strong evidence that J and J' are large enough compared to J'' to give a well-separated $S_T=6$ ground state, and therefore the system does not exhibit spin frustration in the strict sense of degenerate ground states, although there are still competing magnetic interactions created by the topology of the molecule.

UV/Vis spectroscopy of 1–4: The absorption spectra for compounds **1–4** are shown in Figure 11. All four complexes exhibit one main peak in the near-UV region that is not present in the spectrum of the free ligand (Py_2SH in CH_2Cl_2 exhibits a weak band at λ_{max} (ε) 339 nm (41 $M^{-1}\,cm^{-1}$), and intense absorption below 300 nm). The two mononuclear

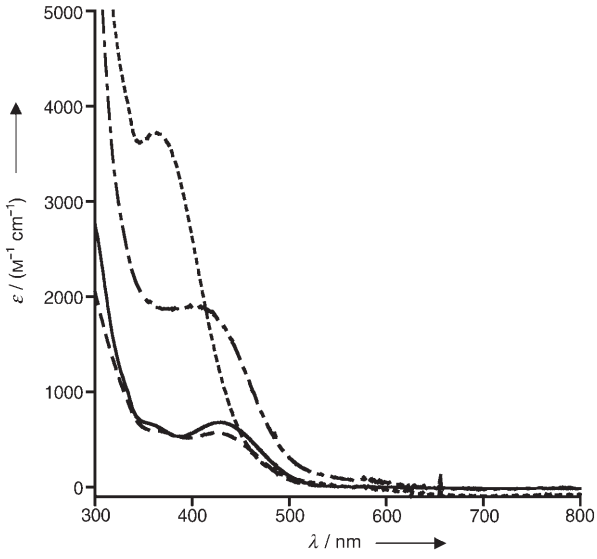

Figure 11. Optical absorption spectra of **1** (solid line), **2** (dashed line), **3** (dotted line) and **4** (broken line) in CH_2Cl_2.

complexes **1** and **2** exhibit spectra that are quite similar, with λ_{max} (ε) 430 nm ($667\,M^{-1}\,cm^{-1}$) for **1** and 422 nm ($572\,M^{-1}\,cm^{-1}$) for **2**. However, the pentanuclear complex **3** shows a significantly blue-shifted and more intense peak at 364 nm ($3770\,M^{-1}\,cm^{-1}$). The dinuclear complex **4** exhibits one main peak in between the peaks for the mononuclear complexes and the pentanuclear complex, at 409 nm ($1847\,M^{-1}\,cm^{-1}$). Although a thorough spectroscopic and theoretical analysis of these transitions has not been carried out thus far, for all three cases these bands can be tentatively assigned to thiolate-to-iron(II) charge-transfer (LMCT) transitions based on their positions, relative intensities, and comparison with RS–Fe^{II} complexes in the literature.[16]

Conclusions and Summary

The ligand Py_2SH, which was used previously only for the synthesis of copper complexes, has been employed in the preparation of the mononuclear, dinuclear, and pentanuclear iron(II) complexes **1**–**4**. Ligands that provide mixed nitrogen/alkylthiolate donation are not common, and Py_2SH is therefore a useful ligand in this regard with respect to the iron(II) ion. The mononuclear complexes **1** and **2** exhibit the five-coordinate geometries expected for TPA-type complexes, but display unusually long N_{amine}–Fe^{II} bonds when compared to other TPA-type species. Their solution state structures match the solid state as revealed by paramagnetic NMR and UV/Vis data.

A method for incorporating OH^- into the coordination sphere of iron(II), which relies upon the use of strict aprotic conditions and a limiting amount of H_2O as the OH^- source, was developed after traditional methods of self-assembly and substitution chemistry failed. This method led to the synthesis of the structurally unprecedented pentanuclear and dinuclear iron(II) complexes **3** and **4**. It was shown that production of **3** or **4** could be controlled by fine-tuning the ligand-to-metal ratio using almost identical reaction conditions.

Magnetic susceptibility studies of **3** and **4** were carried out. In the case of **4**, the two face-sharing, biooctahedral iron(II) ions were found to be antiferromagnetically coupled to give a diamagnetic ground state. From the size of the exchanging coupling (J) and comparisons with the literature it was surmised that the dominant exchange pathway in **4** is likely the thiolate bridges. The magnetic behavior for **3** is significantly more complicated, but was successfully modeled through a spin Hamiltonian method and accompanying DFT calculations. This complex exhibits ferrimagnetic behavior, leading to a high spin $S_T = 6$ ground state. Analysis of the exchange coupling pathways reveals that all of the iron(II) ions couple in an antiferromagnetic manner, but the thiolate bridges provide the dominant interactions and force the iron(II) ions connected by a hydroxide bridge to exhibit parallel spin alignment in the ground state. From the fitting of the data and DFT calculations, it is also concluded that the exchange coupling differs significantly for the different thiolate bridges, even though they are almost identical from a structural perspective.

Experimental Section

General methods: All reactions were carried out under an atmosphere of N_2 or argon using a glovebox or standard Schlenk techniques. All reagents were purchased from commercial vendors and used as received unless noted otherwise. Tetrahydrofuran (THF), diethyl ether, and pentane were distilled under N_2/argon from sodium/benzophenone. Methanol and dichloromethane were distilled over CaH_2. All solvents were further degassed by direct bubbling of argon followed by repeated cycles of freeze-pump-thaw, before storing in a glove box. Sodium hydride (60% in mineral oil) was washed with hexanes prior to use.

UV/Vis spectra were obtained with a Hewlett-Packard 8453 diode array spectrophotometer. Infrared spectra were measured either as KBr pellets or as a thin film on NaCl plates on a Bruker FT-IR spectrometer. Elemental analyses were performed by Atlantic Microlab Inc., Atlanta, GA.

Synthetic procedures: The ligand 1-(bis(2-(pyridin-2-yl)ethyl)amino)-2-methyl propane-2-thiol (Py_2SH) was prepared according to the method published by Ohta et al.[21] The precursor amine, bis(2-pyridylethyl)-amine, was synthesized by two different methods. One method involved the reaction of NH_4Cl and 2-vinyl pyridine in MeOH/water at reflux, following the method developed by Brady et al.[31] It was noticed that a significant side product of this reaction was the primary amine 2-pyridylethylamine, which was isolated during the vacuum distillation of the product. Thus a second method to synthesize Py_2SH involved the reaction of the primary amine with 2-vinyl pyridine. To a solution of the primary amine (7.6 g, 62 mmol) in MeOH was added 2-vinyl pyridine (6.5 g, 62 mmol) and acetic acid (3.6 mL, 62 mmol) and refluxed for 24 h. Standard aqueous workup followed by column chromatography (95:5 CH_2Cl_2/CH_3OH, neutral alumina) resulted in bis(2-pyridylethyl)amine (10.5 g) as an oil.[32] The bis(2-pyridylethyl)amine (7.2 g, 32 mmol) thus obtained was treated with isobutylene sulfide (3.7 mL, 38 mmol), following the method developed by of Ohta et al.[21] to give Py_2SH (5.4 g) as an oil (55%).

[(Py_2S)Fe^{II}Cl] (1): To a stirring solution of Py_2SH (40 mg, 0.126 mmol) in methanol (2.5 mL) was added a methanolic solution (1.5 mL) of NaOH (10.1 mg, 0.253 mmol) and this mixture was allowed to stir for 1 h. A clear solution of the deprotonated thiolate ligand thus obtained was added to $FeCl_2{\cdot}4H_2O$ (25 mg, 0.126 mmol) in methanol (2.5 mL). The resulting yellow solution was allowed to stir for 1.5 h and then filtered through a bed of celite. Diffusion of diethyl ether into the filtrate afforded yellow crystals of **1** (22 mg, 42%). ^1H NMR (500 MHz, CD_2Cl_2): $\delta =$ 90.9, 42.9, 33.9, 32.5, −8.2, −19.0, −24.5 ppm; IR (KBr): $\nu = 2919$, 2853, 1601, 1564, 1445, 1364, 1310, 1268, 1104, 1019, 781, 588 cm^{-1}; UV/Vis (CH_2Cl_2): λ_{max} (ε): 430 nm ($667\,M^{-1}\,cm^{-1}$); elemental analysis calcd (%) for $C_{18}H_{24}ClFeN_3S$ (405.7): C 53.28, H 5.96, N 10.35; found: C 52.81, H 6.02, N 10.19.

[(Py_2S)Fe^{II}Br] (2): To a stirring solution of Py_2SH (40 mg, 0.126 mmol) in methanol (2.5 mL) was added a methanolic solution (1.5 mL) of NaOH (10.1 mg, 0.253 mmol) and this mixture was allowed to stir for 1 h. A clear solution of the deprotonated thiolate ligand thus obtained was added to $FeBr_2$ (27 mg, 0.126 mmol) in methanol (3 mL). The resulting yellow solution was allowed to stir for 1.5 h and then filtered through a bed of celite. Diffusion of diethyl ether into the filtrate afforded yellow crystals of **2** (25 mg, 45%). ^1H NMR (500 MHz, CD_2Cl_2): $\delta = 95.3$, 41.5, 32.5, −15.6, −23.0 ppm; IR (KBr): $\nu = 2956$, 2916, 2862, 1567, 1484, 1444, 1375, 1354, 1314, 1262, 1163, 1147, 1098, 1077, 1061, 1020, 940, 789, 769, 669, 644, 615, 594, 557 cm^{-1}; UV/Vis (CH_2Cl_2): λ_{max} (ε): 422 nm ($572\,M^{-1}\,cm^{-1}$); elemental analysis calcd (%) for $C_{18}H_{24}BrFeN_3S$ (450.2): C 48.01, H 5.37, N 9.33; found: C 48.24, H, 5.36, N 9.36.

Synthesis of [(Py_2S)$_4Fe^{II}_5$(μ-OH)$_2$](BF$_4$)$_4$ (3): To a suspension of NaH (4.8 mg, 0.201 mmol) in THF (2 mL) was added a solution of Py_2SH (53 mg, 0.168 mmol) in THF (2 mL). The suspension went clear and the evolution of gas was noted. The reaction mixture was stirred for 30 min

and then treated with a THF solution (2 mL) of $Fe(BF_4)_2{\cdot}6H_2O$ (56 mg, 0.168 mmol), and a yellow precipitate resulted immediately. The reaction mixture was then stirred for 16 h. The volatiles were removed under vacuum and the resulting yellow solid was redissolved in dichloromethane and filtered through a bed of celite. Brown crystals of **3** (26 mg, 34%) were obtained by diffusion of pentane into the dichloromethane solution of the filtrate. ^{1}H NMR (400 MHz, CD_2Cl_2): $\delta = 94.5$ (br), 64.0 (br), 60.0, 49.0, 41.9, 38.5, 37.0 (br), 36.0, 24.5, 22.0, 18.0 (br), 10.5 (br), −0.5, −1.5, −7.0 (br), −18.0 ppm; IR (thin film): $\nu = 3034$, 2963, 2926, 2863, 1730, 1668, 1568, 1484, 1444, 1364, 1316, 1158, 1052, 875, 665, 646, 594, 520 cm^{-1}; UV/Vis (CH_2Cl_2): λ_{max} (ε): 364 nm ($3770\,M^{-1}\,cm^{-1}$); elemental analysis calcd (%) for $C_{72}H_{98}Fe_5N_{12}S_4O_2B_4F_{16}$ (1918.3): C 45.07, H 5.14, N 8.76; found: C 45.15, H 5.25, N 8.40.

Synthesis of $[(Py_2S)_2Fe^{II}_2(\mu\text{-}OH)]BF_4$ (4): To a suspension of NaH (5.8 mg, 0.244 mmol) in THF (2 mL) was added a solution of Py_2SH (64.3 mg, 0.203 mmol) in THF (2 mL). The suspension went clear and the evolution of gas was noted. The reaction mixture was stirred for 30 min and then treated with a THF solution (2 mL) of $Fe(BF_4)_2{\cdot}6H_2O$ (51.6 mg, 0.152 mmol), and a yellow suspension resulted immediately. The reaction mixture was then stirred for 16 h. The volatiles were removed under vacuum and the resulting yellow solid was redissolved in dichloromethane and filtered through a bed of celite. Orange crystals of **4** (78 mg, 45%) were obtained by diffusion of pentane into the dichloromethane solution of the filtrate. ^{1}H NMR (400 MHz, CD_2Cl_2): $\delta = 79.8$ (br), 41.0, 32.4, −14.2 ppm (br); IR (thin film): $\nu = 3032$, 2957, 2917, 2852, 1723, 1568, 1484, 1379, 1360, 1321, 1262, 1158, 1137, 954, 664, 640 cm^{-1}; UV/Vis (CH_2Cl_2): λ_{max} (ε) 409 nm ($1511\,M^{-1}\,cm^{-1}$); elemental analysis calcd (%) for $C_{36}H_{49}Fe_2N_6S_2OBF_4$ (844.44): C 51.20, H 5.84, N 9.95; found: C 50.59, H 5.72, N 9.65.

Paramagnetic ^{1}H NMR spectroscopy and T_1 measurements: The ^{1}H NMR spectra for the high-spin iron(II) complexes **1** and **2** were measured on a Varian Inova FT-NMR instrument at 500 MHz (^{1}H). The ^{1}H NMR spectrum for complex **3** was measured on a Varian Unity FT-NMR instrument at 400 MHz (^{1}H). Chemical shifts (in ppm) are referenced to the residual solvent peak $CHDCl_2$. Longitudinal relaxation times (T_1) were measured using the inversion–recovery–pulse sequence (180°–τ–90°) method. Crystals of **1** and **2** were isolated from mother liquor and washed repeatedly with Et_2O to remove impurities prior to analysis by NMR. Crystals of **3** were simply isolated from the mother liquor and used directly for NMR experiments.

Magnetic susceptibility studies: Magnetic susceptibility and magnetization measurements on powdered samples were performed on a Cryogenics S600 SQUID magnetometer operating between 0 and 6 T in the range 1.8–300 K. The data were corrected for the diamagnetic contributions using Pascals' constants.

Conductivity: Conductivity measurements were carried out in dichloromethane with an Accumet AR-20 Conductivity meter at 25°C, using an Accumet conductivity cell (cell constant $K = 1.0\,cm^{-1}$). The 1:1 electrolyte $[n\mathrm{Bu_4N}]PF_6$ was used as a standard. The data obtained from the measurements were used to calculate Λ_e, the equivalent conductivity at different concentrations. A plot of Λ_e as a function of the square root of concentration ($c^{1/2}$), followed by extrapolation through a linear least-squares fit resulted in Λ_0, the conductivity at infinite dilution, as the y intercept. Onsager plots were then constructed by plotting the difference, $\Lambda_0 - \Lambda_e$, as a function of $c^{1/2}$.

X-ray crystal structure determinations: Diffraction intensity data were collected with a Bruker Smart Apex CCD diffractometer at 150 K for **1** and **2** and 173 K for **3**. Crystal data, data collection, and refinement parameters are given in Table 6. The space groups for **1**–**3** were chosen based on the systematic absences and intensity statistics. The structures were solved by the direct methods, completed by subsequent difference Fourier syntheses, and refined by full matrix least-squares procedures on F^2. SADABS[75] absorption corrections were applied to the data for **1**–**3**. All non-hydrogen atoms in **1**–**3** were refined with anisotropic displacement coefficients except the B and F atoms of a disordered BF_4^- ion in **3**, which were refined with isotropic thermal parameters. The H atoms in **1** and **2** were found on the Fourier maps and refined with isotropic thermal parameters. The H atoms in **3** were treated as idealized contributions. The Flack parameters for the non-centrosymmetrical structures **1** and **2** are 0.006(9) and 0.005(5), respectively. All software and sources of scat-

Table 6. Crystallographic data for **1**, **2**, **3**·$2\,CH_2Cl_2{\cdot}C_5H_{12}$, and **4**.[a]

	1	**2**	**3**·$2\,CH_2Cl_2{\cdot}C_5H_{12}$	**4**
empirical formula	$C_{18}H_{24}ClFeN_3S$	$C_{18}H_{24}BrFeN_3S$	$C_{79}H_{114}B_4Cl_4F_{16}Fe_5N_{12}O_2S_4$	$C_{36}H_{49}BF_4Fe_2N_6OS_2$
fw	405.76	450.22	2160.36	844.44
T [K]	150(2)	150(2)	173(2)	100
cryst system	orthorhombic	orthorhombic	monoclinic	triclinic
space group	$Pna2_1$	$Pna2_1$	$C2/c$	$P\bar{1}$
a [Å]	14.9482(11)	14.9037(6)	13.0575(16)	12.030(2)
b [Å]	8.9368(6)	8.9422(4)	24.876(3)	12.7114(17)
c [Å]	14.1757(10)	14.4390(6)	31.214(4)	12.806(2)
α [°]	–	–	–	87.467(13)
β [°]	–	–	95.349(2)	89.840(15)
γ [°]	–	–	–	73.306(13)
V [Å^3]	1893.7(2)	1924.3(1)	10095(2)	1873.7(5)
Z	4	4	4	2
color, description	yellow, block	yellow, block	yellow-brown, needle	orange, block
crystal size [mm]	$0.25\times0.20\times0.10$	$0.25\times0.15\times0.10$	$0.48\times0.23\times0.15$	$0.18\times0.11\times0.031$
ρ_{calcd} [g cm^{-3}]	1.423	1.554	1.421	1.497
μ [mm^{-1}]	1.052	2.973	0.968	0.943
absorption correction	SADABS (T_{min}/T_{max})	SADABS (0.880)	SADABS (0.843)	Numerical (0.836)
reflections collected	11020	11156	31819	18888
unique reflections (R_{int})	4311(0.0188)	3814(0.0175)	11523(0.0337)	12201(0.0417)
obsd reflections	4148	3652	7870	7544
$R1$ ($I > 2\sigma(I)$))	0.0215	0.0191	0.0612	0.0561
$wR2$ ($I > 2\sigma(I)$))	0.0501	0.0426	0.1827	0.1402
GOF[2]	1.001	0.992	1.054	0.994
max;min	0.291;−0.218	0.454; −0.181	0.95;−0.94	1.550;−0.915

[a] For all crystal structure determinations $Mo_{K\alpha}$ radiation ($\lambda = 0.71073$ Å) has been used.

tering factors are contained in the SHELXTL (5.10) program package (G.Sheldrick, Bruker XRD, Madison, WI).

Diffraction intensity data were measured with an Oxford Diffraction Xcalibur3 diffractometer equipped with an Enhance (Mo) X-ray Source ($\lambda = 0.71073$ Å) operated at 2 kW power (50 kV, 40 mA) at 100 K for **4**. Crystal data, data collection, and refinement parameters are given in Table 6. The frames were integrated and a face-indexed absorption correction was applied with the Oxford Diffraction CrysAlisRED software package. The space group for **4** was chosen on the basis of the systematic absences and intensity statistics. The structure was solved by direct methods and refined using the Bruker SHELXTL (v6.1) software package. Analysis of the data showed no decay. All non-hydrogen atoms in **4** were refined with anisotropic displacement coefficients; the hydrogen atoms were treated as idealized contributions.

CCDC-263220 (**1**), CCDC-263221 (**2**), CCDC-263219 (**3**), and CCDC-263201 (**4**) contain the supplementary crystallographic data for this paper. These data can be obtained free of charge from the Cambridge Crystallographic Data Centre via www.ccdc.cam.ac.uk/data_request/cif.

Acknowledgements

We are grateful to the National Institutes of Health (GM62309 to D.P.G.) for support of this work. D.P.G. also acknowledges the Alfred P. Sloan, Jr. Foundation. We also thank Dr. Ananya Majumdar for assistance with NMR measurements. A.C. and F.T. acknowledge grants from Italian MIUR, FIRB project, and E.C. RTN, QUEMOLNA, FP6–504880.

[1] G. Parkin, *Chem. Rev.* **2004**, *104*, 699–767.
[2] V. V. Karambelkar, D. Krishnamurthy, C. L. Stern, L. Zakharov, A. L. Rheingold, D. P. Goldberg, *Chem. Commun.* **2002**, 2772–2773.
[3] S. C. Chang, V. V. Karambelkar, R. D. Sommer, A. L. Rheingold, D. P. Goldberg, *Inorg. Chem.* **2002**, *41*, 239–248.
[4] S. Chang, R. D. Sommer, A. L. Rheingold, D. P. Goldberg, *Chem. Commun.* **2001**, 2396–2397.
[5] J. N. Smith, Z. Shirin, C. J. Carrano, *J. Am. Chem. Soc.* **2003**, *125*, 868–869.
[6] B. Benkmil, M. Ji, H. Vahrenkamp, *Inorg. Chem.* **2004**, *43*, 8212–8214.
[7] J. Seebacher, M. H. Shu, H. Vahrenkamp, *Chem. Commun.* **2001**, 1026–1027.
[8] J. J. Smee, M. L. Miller, C. A. Grapperhaus, J. H. Reibenspies, M. Y. Darensbourg, *Inorg. Chem.* **2001**, *40*, 3601–3605.
[9] C. A. Grapperhaus, M. Y. Darensbourg, *Acc. Chem. Res.* **1998**, *31*, 451–459.
[10] V. E. Kaasjager, E. Bouwman, S. Gorter, J. Reedijk, C. A. Grapperhaus, J. H. Reibenspies, J. J. Smee, M. Y. Darensbourg, A. Derecskei-Kovacs, L. M. Thomson, *Inorg. Chem.* **2002**, *41*, 1837–1844.
[11] M. L. Golden, M. V. Rampersad, J. H. Reibenspies, M. Y. Darensbourg, *Chem. Commun.* **2003**, 1824–1825.
[12] C. A. Grapperhaus, C. S. Mullins, P. M. Kozlowski, M. S. Mashuta, *Inorg. Chem.* **2004**, *43*, 2859–2866.
[13] J. A. Kovacs, *Chem. Rev.* **2004**, *104*, 825–848.
[14] J. Shearer, R. C. Scarrow, J. A. Kovacs, *J. Am. Chem. Soc.* **2002**, *124*, 11709–11717.
[15] S. C. Shoner, D. Barnhart, J. A. Kovacs, *Inorg. Chem.* **1995**, *34*, 4517–4518.
[16] J. A. Halfen, H. L. Moore, D. C. Fox, *Inorg. Chem.* **2002**, *41*, 3935–3943.
[17] T. C. Harrop, P. K. Mascharak, *Acc. Chem. Res.* **2004**, *37*, 253–260.
[18] J. C. Noveron, M. M. Olmstead, P. K. Mascharak, *J. Am. Chem. Soc.* **2001**, *123*, 3247–3259.
[19] C. A. Grapperhaus, M. Li, A. K. Patra, S. Poturovic, P. M. Kozlowski, M. Z. Zgierski, M. S. Mashuta, *Inorg. Chem.* **2003**, *42*, 4382–4388.
[20] F. M. Macdonnell, K. Ruhlandtsenge, J. J. Ellison, R. H. Holm, P. P. Power, *Inorg. Chem.* **1995**, *34*, 1815–1822.
[21] T. Ohta, T. Tachiyama, K. Yoshizawa, T. Yamabe, T. Uchida, T. Kitagawa, *Inorg. Chem.* **2000**, *39*, 4358–4369.
[22] T. Ohta, T. Tachiyama, K. Yoshizawa, T. Yamabe, *Tetrahedron Lett.* **2000**, *41*, 2581–2585.
[23] S. C. Shoner, A. M. Nienstedt, J. J. Ellison, I. Y. Kung, D. Barnhart, J. A. Kovacs, *Inorg. Chem.* **1998**, *37*, 5721–5726.
[24] J. A. Halfen, H. L. Halfen, T. C. Brunold, A. T. Fiedler, *J. Am. Chem. Soc.* **2005**, *127*, 1675.
[25] D. K. Garner, S. B. Fitch, L. H. McAlexander, L. M. Bezold, A. M. Arif, L. M. Berreau, *J. Am. Chem. Soc.* **2002**, *124*, 9970–9971.
[26] B. M. Bridgewater, G. Parkin, *Inorg. Chem. Commun.* **2001**, *4*, 126–129.
[27] R. Alsfasser, S. Trofimenko, A. Looney, G. Parkin, H. Vahrenkamp, *Inorg. Chem.* **1991**, *30*, 4098–4100.
[28] A. Looney, R. Han, K. Mcneill, G. Parkin, *J. Am. Chem. Soc.* **1993**, *115*, 4690–4697.
[29] S. Hikichi, T. Ogihara, K. Fujisawa, N. Kitajima, M. Akita, Y. Moro-Oka, *Inorg. Chem.* **1997**, *36*, 4539–4547.
[30] N. Kitajima, N. Tamura, M. Tanaka, Y. Morooka, *Inorg. Chem.* **1992**, *31*, 3342–3343.
[31] L. E. Brady, M. Freifelder, G. R. Stone, *J. Org. Chem.* **1961**, *26*, 4757–4758.
[32] E. Gojon, P. Dubourdeaux, N. Gon, J. M. Latour, *New J. Chem.* **1988**, *12*, 931–939.
[33] D. Mandon, A. Machkour, S. Goetz, R. Welter, *Inorg. Chem.* **2002**, *41*, 5364–5372.
[34] Y. Zang, L. Que, Jr., *Inorg. Chem.* **1995**, *34*, 1030–1035.
[35] R. N. Mukherjee, A. J. Abrahamson, G. S. Patterson, T. D. P. Stack, R. H. Holm, *Inorg. Chem.* **1988**, *27*, 2137–2144.
[36] Y. M. Chiou, L. Que, Jr., *J. Am. Chem. Soc.* **1995**, *117*, 3999–4013.
[37] A. Diebold, K. S. Hagen, *Inorg. Chem.* **1998**, *37*, 215–223.
[38] F. H. Allen, *Acta Crystallogr. Sect. B* **2002**, *58*, 380–388.
[39] See for example: a) X. D. Xu, C. S. Allen, C. L. Chuang, J. W. Canary *Acta Crystallogr. C* **1998**, *54*, 600 and b) E. H. Alilou, A. E. Hallaoui, E. H. E. Ghadraoui, M. Giorgi, M. Pierrot, M. Reglier, *Acta Crystallogr. Sect. C* **1997**, *53*, 559.
[40] A. W. Addison, T. N. Rao, J. Reedjik, J. van Rijn, G. C. Verschoor, *J. Chem. Soc. Dalton Trans.* **1984**, 1349–1456.
[41] A. L. Gavrilova, B. Bosnich, *Chem. Rev.* **2004**, *104*, 349–383.
[42] R. S. Drago, *Physical Methods for Chemists*, 2nd ed., Saunders College Publishing, **1992**, p. 500.
[43] R. Alsfasser, M. Ruf, S. Trofimenko, H. Vahrenkamp, *Chem. Ber-Recl* **1993**, *126*, 703–710.
[44] For the self-assembly of a related calixarene zinc-aqua species, see: O. Seneque, M. N. Rager, M. Giorgi, O. Reinaud, *J. Am. Chem. Soc.* **2001**, *123*, 8442–8443.
[45] V. L. MacMurdo, H. Zheng, L. Que, Jr., *Inorg. Chem.* **2000**, *39*, 2254–2255.
[46] R. A. Reynolds, W. O. Yu, W. R. Dunham, D. Coucouvanis, *Inorg. Chem.* **1996**, *35*, 2721–2722.
[47] D. R. Evans, R. S. Mathur, K. Heerwegh, C. A. Reed, Z. W. Xie, *Angew. Chem.* **1997**, *109*, 1394–1396; *Angew. Chem. Int. Ed. Engl.* **1997**, *36*, 1335–1337.
[48] W. R. Scheidt, B. Cheng, M. K. Safo, F. Cukiernik, J. C. Marchon, P. G. Debrunner, *J. Am. Chem. Soc.* **1992**, *114*, 4420–4421.
[49] S. C. Payne, K. S. Hagen, *J. Am. Chem. Soc.* **2000**, *122*, 6399–6410.
[50] J. A. R. Hartman, R. L. Rardin, P. Chaudhuri, K. Pohl, K. Wieghardt, B. Nuber, J. Weiss, G. C. Papaefthymiou, R. B. Frankel, S. J. Lippard, *J. Am. Chem. Soc.* **1987**, *109*, 7387–7396.
[51] W. J. Geary, *Coord. Chem. Rev.* **1971**, *7*, 81–122.
[52] J. F. Coetzee, G. P. Cunningham, *J. Am. Chem. Soc.* **1965**, *87*, 2529–2534.
[53] R. D. Feltham, R. G. Hayter, *J. Chem. Soc.* **1964**, 4587–4591.
[54] T. Chandra, R. A. Allred, B. J. Kraft, L. M. Berreau, J. M. Zaleski, *Inorg. Chem.* **2004**, *43*, 411–420.
[55] Y. H. Chiu, J. W. Canary, *Inorg. Chem.* **2003**, *42*, 5107–5116.

[56] B. Kersting, D. Siebert, D. Volkmer, M. J. Kolm, C. Janiak, *Inorg. Chem.* **1999**, *38*, 3871–3882.
[57] F. A. Cotton, D. A. Ucko, *Inorg. Chim. Acta* **1972**, *6*, 161–172.
[58] R. H. Summerville, R. Hoffmann, *J. Am. Chem. Soc.*, **1979**, *101*, 3821–3831.
[59] M. Mikuriya, T. Kotera, F. Adachi, M. Handa, M. Koikawa, H. Okawa, *Bull. Chem. Soc. Jpn.* **1995**, *68*, 574–580.
[60] U. Bossek, D. Nühlen, E. Bill, T. Glaser, C. Krebs, T. Weyhermüller, K. Wieghardt, M. Lengen, A. X. Trautwein, *Inorg. Chem.* **1997**, *36*, 2834–2843.
[61] Z. Janas, P. Sobota, T. Lis, *J. Chem. Soc. Dalton* **1991**, 2429–2434.
[62] J. D. Lawrence, T. B. Rauchfuss, S. R. Wilson, *Inorg. Chem.* **2002**, *41*, 6193–6195.
[63] L. Toma, R. Lescouezec, J. Vaissermann, F. S. Delgado, C. Ruiz-Perez, R. Carrasco, J. Cano, F. Lloret, M. Julve, *Chem. Eur. J.* **2004**, *10*, 6130–6145.
[64] G. Aromi, C. Boldron, P. Gamez, O. Roubeau, H. Kooijman, A. L. Spek, H. Stoeckli-Evans, J. Ribas, J. Reedijk, *Dalton Trans.* **2004**, 3586.
[65] D. Gatteschi, A. Caneschi, R. Sessoli, A. Cornia, *Chem. Soc. Rev.* **1996**, *25*, 101.
[66] D. R. Gamelin, E. L. Bominaar, M. L. Kirk, K. Wieghardt, E. I. Solomon, *J. Am. Chem. Soc.* **1996**, *118*, 8085–8097.
[67] D. Gatteschi, L. Pardi, *Gazz. Chim. Ital.* **1993**, *123*, 231.
[68] L. Noodleman, J. G. J. Norman, *J. Chem. Phys.* **1979**, *70*, 4903–4906.
[69] L. Noodleman, *J. Chem. Phys.* **1981**, *74*, 5737–5743.
[70] T. P. Straatsma, E. Apra′, T. L. Windus, M. Dupuis, E. J. Bylaska, W. de Jong, S. Hirata, D. M. A. Smith, M. Hackler, L. Pollack, R. Harrison, J. Nieplocha, T. V., M. Krishnan, E. Brown, G. Cisneros, G. Fann, H. Fruchtl, J. Garza, K. Hirao, R. Kendall, J. Nichols, K. Tsemekhman, M. Valiev, K. Wolinski, J. Anchell, D. Bernholdt, P. Borowski, T. Clark, D. Clerc, H. Dachsel, M. Deegan, K. Dyall, D. Elwood, E. Glendening, M. Gutowski, A. Hess, J. Jaffe, B. Johnson, J. Ju, R. Kobayashi, R. Kutteh, Z. Lin, R. Littlefield, X. Long, B. Meng, T. Nakajima, S. Niu, M. Rosing, G. Sandrone, M. Stave, H. Taylor, G. Thomas, J. van Lenthe, A. Wong, Z. Zhang, "NWChem, A Computational Chemistry Package for Parallel Computers, v. 4.5" (2003), Pacific Northwest National Laboratory, Richland, Washington 99352–0999, USA.
[71] R. A. Kendall, E. Apra, D. E. Bernholdt, E. J. Bylaska, M. Dupuis, G. I. Fann, R. J. Harrison, J. L. Ju, J. A. Nichols, J. Nieplocha, T. P. Straatsma, T. L. Windus, A. T. Wong, *Comput. Phys. Commun.* **2000**, *128*, 260. See references therein for the Ahlrichs TZV/VDZ basis sets and for the B3LYP functional.
[72] A. Bencini, F. Totti, *Int. J. Quantum Chem.* **2005**, *101*, 819.
[73] E. Libby, J. K. McCusker, E. A. Schmitt, K. Folting, D. N. Hendrickson, G. Christou, *Inorg. Chem.* **1991**, *30*, 3486–3495.
[74] O. Kahn, *Molecular Magnetism*, VCH Publishers, New York, **1993**.
[75] G. M. Sheldrick, SADABS (2.01), Bruker/Siemens Area Detector Absorption Correction Program, Bruker AXS, Madison, Wisconsin, USA, **1998**.

Received: February 12, 2005
Published online: September 6, 2005

